energies

MDPI

Article

# Characterizing Flexoelectricity in Composite Material Using the Element-Free Galerkin Method

**Bo He [3,4], Brahmanandam Javvaji [4] and Xiaoying Zhuang [1,2,*]**

1 Division of Computational Mechanics, Ton Duc Thang University, 700000 Ho Chi Minh City, Viet Nam
2 Faculty of Civil Engineering, Ton Duc Thang University, 700000 Ho Chi Minh City, Viet Nam
3 College of Civil Engineering, Tongji University, 1239 Siping Road, Shanghai 200092, China; bohe@ikm.uni-hannover.de
4 Institute of Continuum Mechanics, Leibniz Universität Hannover, Appelstr. 11, 30167 Hannover, Germany; brahmanandam@ikm.uni-hannover.de
* Correspondence: xiaoying.zhuang@tdtu.edu.vn

Received: 30 October 2018; Accepted: 11 December 2018; Published: 16 January 2019


**Abstract:** This study employs the Element-Free Galerkin method (EFG) to characterize flexoelectricity in a composite material. The presence of the strain gradient term in the Partial Differential Equations (PDEs) requires $C^1$ continuity to describe the electromechanical coupling. The use of quartic weight functions in the developed model fulfills this prerequisite. We report the generation of electric polarization in a non-piezoelectric composite material through the inclusion-induced strain gradient field. The level set technique associated with the model supervises the weak discontinuity between the inclusion and matrix. The increased area ratio between the inclusion and matrix is found to improve the conversion of mechanical energy to electrical energy. The electromechanical coupling is enhanced when using softer materials for the embedding inclusions.

**Keywords:** flexoelectricity; meshless method; composite; size effect; level set technique

## 1. Introduction

An energy harvester utilizing the electromechanical coupling effect has been applied in various applications, ranging from sensors [1–3] to biomedical devices [4,5] at both micro- and nano-scales [6–8]. The well-known electromechanical coupling effect, piezoelectricity, generates the electrical polarization under mechanical deformation only in the non-centrosymmetric material. Flexoelectricity is another type of electromechanical coupling, which describes the coupling between the electrical potential and strain gradient. Unlike piezoelectricity, flexoelectricity can exist in any dielectric material regardless of the material's inner structure. In the meantime, experimental studies [9,10] observed an unexpected giant flexoelectric effect in barium strontium titanate, which suggested that at the micro-/nano-scale, the flexoelectric effect outperforms the piezoelectric effect. These superior properties of flexoelectricity at a small scale have drawn extensive research attention towards the fundamental investigation of this electromechanical coupling from the molecular scale to the continuum scale. Atomic-level density functional theories [11–13] and molecular dynamics simulations [14,15] explored the mechanism of inducing flexoelectric polarization under deformation. However, continuum scale studies can lead to better understanding of the practical applicability of the flexoelectric property in designing sensors and actuators.

The characterization of flexoelectricity with existing numerical methods, like the Finite Element Method (FEM), requires remarkable modifications to handle the strain gradient term. Zhang et al. [16] used conventional FEM to evaluate the piezo- and flexo-electric effects by solving the partial differential equations for the displacement and electric potential in a decoupled manner. The conventional

FEM works on the basis of $C^0$ continuity and is uncertain when higher order strain terms are present (challenging to hold $C^1$ continuity). Nanthakumar et al. [17,18] used the Mixed Finite Element Formulation (MFEF) to maximize the flexoelectric effect through topology optimization of barium titanate material. However, the MFEF method suffers from high computational cost [19,20]. Isogeometric Analysis (IGA) is another numerical method, which ensures the required $C^1$ continuity by employing the higher-order shape functions [21–23]; whereas, IGA strongly depends on the geometrical symmetry conditions to reduce the computational cost [24,25]. Abdollahi et al. [26,27] developed a meshless method to study the flexoelectric response of dielectric material both in cantilever beam and truncated pyramid shapes. Their study further suggested that the simplified analytical model is unable to capture the flexoelectricity in multi-dimensional geometries. These studies have used structures with a ceramic material such as barium titanate or strontium titanate. Applications of these materials have a limited scope due to the small operational strain and high-stress conditions [28].

Experimental studies revealed that composites made up of two or many materials are promising to support high stress operating conditions. For example, nano-indentation tests of a bilayer cantilever beam structure have shown good mechanical properties [29,30]. A study on the polymer-based composite with graphene oxide has shown enhanced piezoelectric performance with greater flexibility [31]. Synthesized polymeric composite with piezoelectric zirconia titanate material promised to exhibit good energy-harvesting solutions [32]. However, these findings critically depend on the piezoelectric properties of the material. On the other hand, it is possible to create the piezoelectric composites without using a material with piezoelectric properties. The flexoelectric fiber-reinforced composite [33,34] and multi-material-based flexoelectric composites [35] are some example studies in this direction. The flexoelectric composites develop large strain gradients near the material discontinuity when uniformly deformed, which generates the electrical polarization through flexoelectricity. However, the numerical modeling other than conventional FEM requires extra care when dealing with the material and geometry discontinuity between the composite constituents. Lagrange multipliers [36,37] and the global enrichment approach [38,39] are the few techniques to treat the material discontinuity. The applicability of these methods is cumbersome when using complex geometries in 2D structures [40,41]. The Extended Finite Element Method (XFEM) has been used for the level set technique to describe the weak discontinuity between the inclusion and matrix composite [42–44]. In addition, the level set technique also allows using the multiple randomly-distributed inclusions inside the matrix.

The current work employs the Element-Free Galerkin (EFG) method [45–49] along with the level set technique to characterize flexoelectricity in a composite. It is assumed that the composite is a combination of embedding matrix material and a non-piezoelectric material (inclusion). The possible generation of electrical voltage due to the compressive loading of the composite is investigated. This study is extended to find the dependence of the electrical voltage on the concentration of inclusions in the embedding matrix. The numerical model is validated with standard examples and then utilized to explore the flexoelectricity in a composite. Section 2 composes the details of the EFG. Numerical validation and example case studies are presented in Section 3. Section 4 concludes the work.

## 2. Simulation Method

The enthalpy density $\mathcal{H}$ for a dielectric solid with the piezoelectric and flexoelectric effect is [50–52]:

$$\mathcal{H}(\epsilon_{ij}, E_i, \epsilon_{jk,l}, E_{i,j}) = \frac{1}{2}\mathbb{C}_{ijkl}\epsilon_{ij}\epsilon_{kl} - e_{ikl}E_i\epsilon_{kl} - \mu_{ijkl}E_i\epsilon_{jk,l} - \frac{1}{2}\kappa_{ij}E_iE_j\,, \tag{1}$$

where $E_i = -\phi_{,i}$ is the electric field; $\phi_i$ being the electric potential in the $i$ direction; $\epsilon_{ij}$ is the mechanical strain; $\mathbb{C}_{ijkl}$ is the fourth-order elastic moduli tensor; $e_{ikl}$ is the third-order tensor of piezoelectricity; $\mu_{ijkl}$ is the fourth-order flexoelectric tensor; and $\kappa_{ij}$ is the second-order dielectric tensor. Appendix A covers further details about the weak form of Equation (1) and possible boundary conditions. The resulting governing equations are solved for unknown variables displacement $\boldsymbol{u}$

and electric potential $\boldsymbol{\phi}$ using Moving Least Squares approximation (MLS). Belytschko et al. [53–55] introduced the MLS approximation within the EFG. According to the MLS, the unknowns ($\boldsymbol{u}$ and $\boldsymbol{\phi}$) for the center node are approximated by the neighboring nodes in its support domain (Figure 1a). If the support domain encounters a material discontinuity, corresponding support nodes are enriched. The weak discontinuity across the material interface in the composite is modeled with the level set function with absolute sign distance function $\Psi(x)$. Figure 1b shows the schematic illustration of the level set function and its first-order-derivative across the interface. The local approximation of displacement $\boldsymbol{u}$ and electric potential $\boldsymbol{\phi}$ at location x are given as:

$$\begin{aligned} \boldsymbol{u}^h(x) &= \sum_{I=1}^{N} \Phi_I(x)\boldsymbol{u}_I + \sum_{I=J}^{M} \Phi_J(x)\Psi(x)\boldsymbol{u}_J; \\ \phi^h(x) &= \sum_{I=1}^{N} \Phi_I(x)\phi_I + \sum_{I=J}^{M} \Phi_J(x)\Psi(x)\phi_J, \end{aligned} \tag{2}$$

where $\Phi(x)$ is the shape function at position $x$, $\boldsymbol{u}$ and $\phi$ are the nodal displacements and electric potential, and $N$ and $M$ are the number of support and enriched nodes, respectively. More details about $\Phi(x)$ are given in Appendix B. Hereafter, we write the approximation in a simplified form $\boldsymbol{u}^h = \boldsymbol{\Phi}_u\boldsymbol{u}^{std} + \boldsymbol{\Phi}_u\boldsymbol{\Psi}\boldsymbol{u}^{enr}$. The derivatives for unknowns $\boldsymbol{u}$ and $\boldsymbol{\phi}$ (Equation (2)) contribute by both support nodes ($\boldsymbol{u}^{std}$, $\boldsymbol{\phi}^{std}$) and enriched nodes ($\boldsymbol{u}^{enr}$, $\boldsymbol{\phi}^{enr}$ ), which are given as:

$$\begin{aligned} \frac{\partial \boldsymbol{u}^h}{\partial x} &= \frac{\partial \boldsymbol{\Phi}_u}{\partial x}\boldsymbol{u}^{std} + \frac{\partial \boldsymbol{\Phi}_u}{\partial x}\boldsymbol{\Psi}\boldsymbol{u}^{enr} + \boldsymbol{\Phi}_u\frac{\partial \boldsymbol{\Psi}}{\partial x}\boldsymbol{u}^{enr}; \\ \frac{\partial^2 \boldsymbol{u}^h}{\partial x^2} &= \frac{\partial^2 \boldsymbol{\Phi}_u}{\partial x^2}\boldsymbol{u}^{std} + \frac{\partial^2 \boldsymbol{\Phi}_u}{\partial x^2}\boldsymbol{\Psi}\boldsymbol{u}^{enr} + \boldsymbol{\Phi}_u\frac{\partial^2 \boldsymbol{\Psi}}{\partial x^2}\boldsymbol{u}^{enr} + 2\frac{\partial \boldsymbol{\Phi}_u}{\partial x}\frac{\partial \boldsymbol{\Psi}}{\partial x}\boldsymbol{u}^{enr}; \\ \frac{\partial \phi^h}{\partial x} &= \frac{\partial \boldsymbol{\Phi}_\phi}{\partial x}\boldsymbol{\phi}^{std} + \frac{\partial \boldsymbol{\Phi}_\phi}{\partial x}\boldsymbol{\Psi}\boldsymbol{\phi}^{enr} + \boldsymbol{\Phi}_\phi\frac{\partial \boldsymbol{\Psi}}{\partial x}\boldsymbol{\phi}^{enr}. \end{aligned} \tag{3}$$

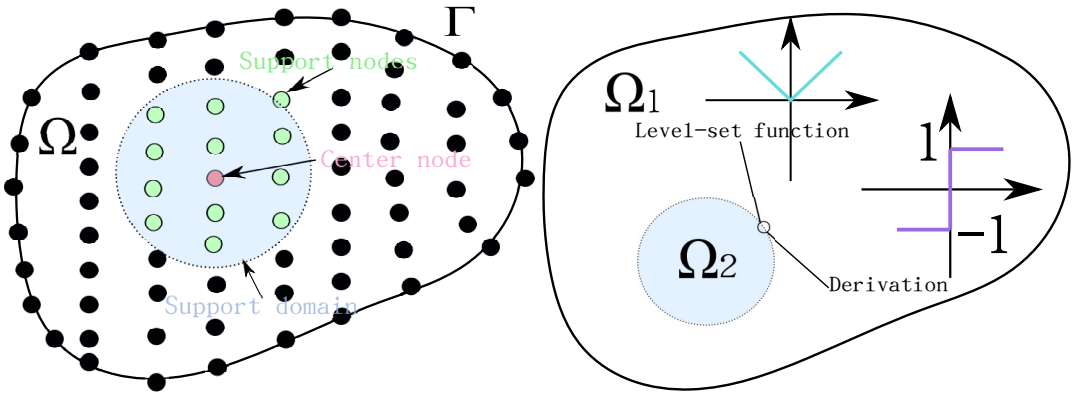


(**a**) Schematic illustration of MLS approximation, (**b**) Level-set function and its derivation cross the interface

**Figure 1.** (**a**) Schematic illustration of Moving Least Squares (MLS) approximation and (**b**) the level-set function and its derivation across the interface.

The discrete equilibrium equations involving Equation (3) are given as:

$$\begin{bmatrix} A_{uu} & A_{u\phi} \\ A_{u\phi}^T & A_{\phi\phi} \end{bmatrix} \cdot \begin{bmatrix} \boldsymbol{u} \\ \boldsymbol{\phi} \end{bmatrix} = \begin{bmatrix} \boldsymbol{f_u} \\ \boldsymbol{f_\phi} \end{bmatrix}, \tag{4}$$

where:

$$A_{uu} = \sum_e \int_{\Omega_e} (\boldsymbol{B}_u + \boldsymbol{B}_u^{enr})\mathbb{C}(\boldsymbol{B}_u + \boldsymbol{B}_u^{enr})^T d\Omega_e; \tag{5}$$

$$A_{u\phi} = \sum_e \int_{\Omega_e} \left( (\boldsymbol{B}_u + \boldsymbol{B}_u^{enr}) \boldsymbol{e} (\boldsymbol{B}_\phi + \boldsymbol{B}_\phi^{enr})^T + (\boldsymbol{H}_u + \boldsymbol{H}_u^{enr}) \boldsymbol{\mu}^T (\boldsymbol{B}_\phi + \boldsymbol{B}_\phi^{enr})^T \right) d\Omega_e; \tag{6}$$

$$A_{\phi\phi} = -\sum_e \int_{\Omega_e} (\boldsymbol{B}_\phi + \boldsymbol{B}_\phi^{enr}) \boldsymbol{\kappa} (\boldsymbol{B}_\phi + \boldsymbol{B}_\phi^{enr})^T d\Omega_e; \tag{7}$$

$$\boldsymbol{f_u} = \sum_e \int_{\Gamma_t e} \boldsymbol{N}_u^T \boldsymbol{t}_\Gamma d\Gamma_{te}; \tag{8}$$

$$\boldsymbol{f_\phi} = -\sum_e \int_{\Gamma_D e} \boldsymbol{N}_\phi^T \boldsymbol{w} d\Gamma_{De}; \tag{9}$$

where $e$ refers to element number. Further details about the individual $\boldsymbol{B}$ and $\boldsymbol{H}$ matrices are included in Appendix C. The Lagrange multiplier method is used for imposing mechanical and electrical boundary conditions. In this study, the plane strain condition is assumed. Material property matrices $\mathbb{C}$, $\boldsymbol{\kappa}$, $\boldsymbol{e}$, $\boldsymbol{\mu}$ are given as:

$$\mathbb{C} = \frac{E}{(1+\nu)(1-2\nu)} \begin{bmatrix} 1-\nu & \nu & 0 \\ \nu & 1-\nu & 0 \\ 0 & 0 & (\frac{1}{2}-\nu) \end{bmatrix}, \tag{10}$$

$$\boldsymbol{\kappa} = \begin{bmatrix} k_{11} & 0 \\ 0 & k_{33} \end{bmatrix}, \tag{11}$$

$$\boldsymbol{e^T} = \begin{bmatrix} 0 & 0 & e_{15} \\ e_{31} & e_{33} & 0 \end{bmatrix}, \tag{12}$$

$$\boldsymbol{\mu} = \begin{bmatrix} \mu_{11} & \mu_{12} & 0 & 0 & 0 & \mu_{44} \\ 0 & 0 & \mu_{44} & \mu_{12} & \mu_{11} & 0 \end{bmatrix}. \tag{13}$$

## 3. Numerical Examples

In this section, we validate the numerical model with benchmark problems: electromechanical characteristics of a cantilever beam under mechanical and electrical loading conditions and coupling effects in a mechanically-compressed truncated pyramid. Note that these problems are free from the material discontinuity. The obtained results are validated with the reported literature. The complete numerical model with material discontinuity and local enrichment is employed to estimate the characteristics of the composite material.

### *3.1. Cantilever Beam*

Figure 2a,b shows the simulation setup for open circuit mechanical loading and close circuit electrical loading, respectively. The length to thickness ratio $L/h$ for the cantilever beam is 20. Table 1 reports the various material parameters [21].

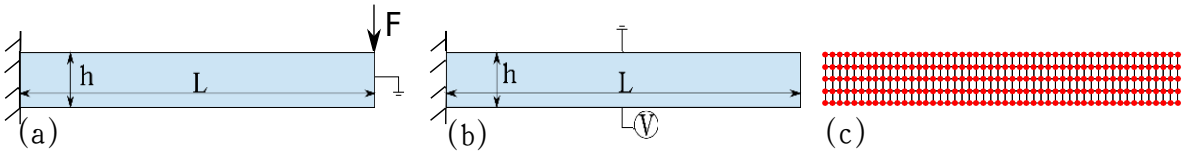


**Figure 2.** Schematic illustration of the cantilever beam under (**a**) mechanical loading and (**b**) electrical loading. (**c**) MLS discretization with the red solid point representing the nodes.

**Table 1.** Material properties.

| Name | Symbol | Value |
|---|---|---|
| Poisson's ratio | $\nu$ | 0.37 |
| Young's modulus | E | 100 GPa |
| Piezoelectric constant | $e_{31}$ | $-4.4$ nC/m$^2$ |
| Flexoelectric constant | $\mu_{12}$ | 1 µC/m |
| Dielectric constant | $\kappa_{11}$; $\kappa_{33}$ | 11 nC/Vm; 12.48 nC/Vm |
| Electric susceptibility | $\chi$ | 1408 |

#### 3.1.1. Mechanical Loading

A point load $F = 100$ µN is applied on the upper right edge of the cantilever beam (Figure 2a), and the electric potential is constrained to zero. Electromechanical coupling induces the electrical energy under point load deformation. The conversion from mechanical to electrical energy ($k^2_{eff}$) is defined as:

$$k^2_{eff} = \frac{W_{elec}}{W_{mech}} = \frac{\int \boldsymbol{E} \cdot \kappa \cdot \boldsymbol{E}}{\int \epsilon : \mathbb{C} : \epsilon}. \tag{14}$$

The present model is simplified by assuming that the transversal piezoelectric ($e = e_{31}$) and flexoelectric ($\mu = \mu_{12}$) components are the only non-zero in Equations (12) and (13). The Poisson effect is also ignored. The results of this simplified model are compared with the analytical model derived by Majdoub et al. [50]. The analytical solution for $k_{eff}$ is:

$$k_{eff} = \frac{\chi}{1+\chi}\sqrt{\frac{\kappa}{Y}(e^2 + 12\left(\frac{\mu}{h}\right)^2)}, \tag{15}$$

where the normalized piezoelectric constant is:

$$e' = \frac{k_{eff}}{k_{piezo}}, \tag{16}$$

where $k_{piezo}$ is obtained by neglecting flexoelectricity coefficient $\mu$ in Equation (15).

Figure 3a plots the comparison between the present model and the analytical solution, where $h' = -eh/\mu$ is the normalized beam thickness for the open circuit mechanical loading condition. The variation between $e'$ and $h'$ from the present model agrees with the analytical solution from Equation (16). This proves that the present model correctly estimates the electromechanical coupling in a non-piezoelectric beam under bending deformation. The coupling between mechanical and electric energy is strongly mediated by the flexoelectricity due to the low piezoelectric constant of the material (refer to Table 1). Figure 3b shows the distribution of the generated electric potential under the flexoelectric effect.

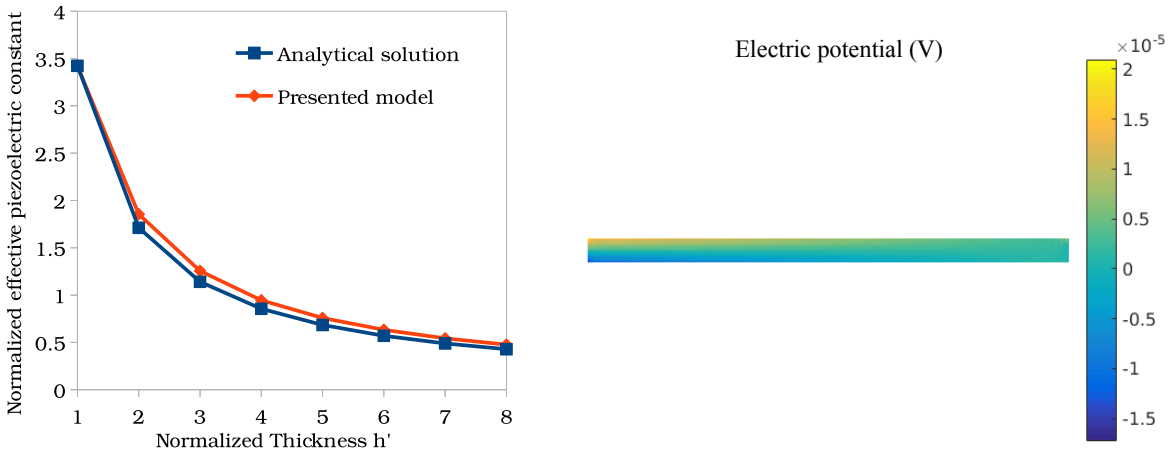


(**a**) Size-dependent effective piezoelectric constant (**b**) Electric potential (V)

**Figure 3.** Calculation results of the (**a**) size-dependent effective piezoelectric constant and (**b**) the electric potential profile for a fully-coupled cantilever beam.

### 3.1.2. Electrical Loading

In this section, we study a cantilever beam (Figure 2b) under pure electric loading, which served as an actuator. The bottom edge of the cantilever beam (Figure 2b) enforced an electrical loading of $-20$V and grounded the top edge. There is no external mechanical loading in the cantilever beam. Figure 4 displays the displacement and electric potential profiles. The electric field across the beam in the $y$-direction is plotted in Figure 5. The electric field gradients near the top (negative sign) and bottom (positive sign) surface of the cantilever beam are due to the effect of converse flexoelectricity. This phenomenon generates mechanical stress at the top and bottom surface and thus deforms the beam. The displacement and electric potential distribution on the cantilever beam are in good agreement with earlier findings based on IGA analysis [21].

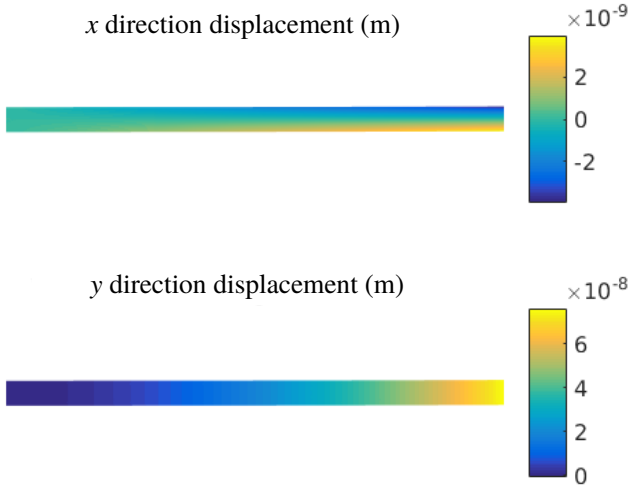


(**a**) Displacement in the x and y directions (m)

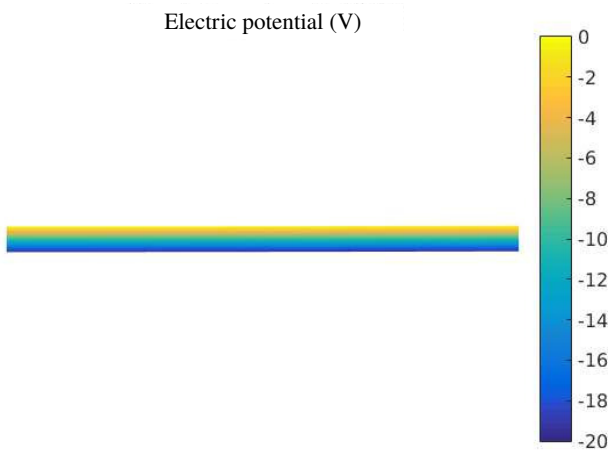


(**b**) Electric potential (V)

**Figure 4.** Calculation result of the cantilever beam under electric loading: (**a**) beam displacement; (**b**) electric potential profile.

### *3.2. Compress Truncated Pyramid*

In this section, we have extended the validation for the compression of a truncated pyramid (Figure 6). Due to its different top ($a_1$) and bottom ($a_2$) edge lengths, the applied uniform force $F$ generates different tractions at the top and bottom edges, which results in a longitudinal strain gradient. The top edge of the pyramid is grounded, and a uniform force of $-6e6$ N is applied to it. The aspect ratio $h$ of the pyramid is set as 75 µm, and the bottom edge length is 225 µm. The remaining material parameters are listed in Table 1. Figure 7 shows the developed strain in the $y$-direction and the electromechanical coupling-induced electric potential profiles. The numerical values and the field distributions are in good agreement with earlier reports [21]. This represents that the present model accurately estimated the electromechanical coupling.

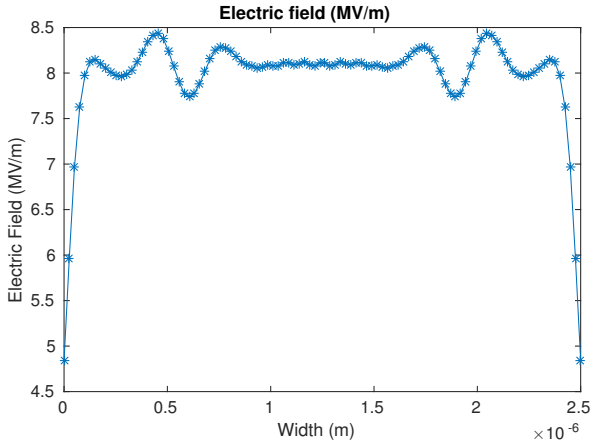


**Figure 5.** Calculation result of the electric field profile across the beam in the y direction at the mid-length of the beam.

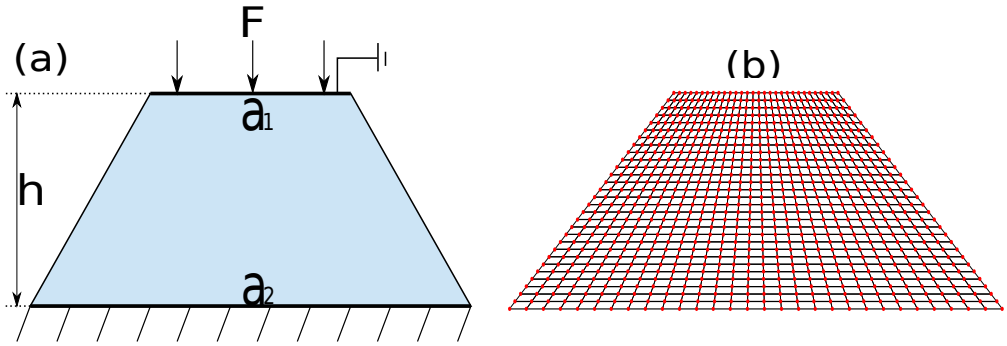


**Figure 6.** Schematic illustration of: (**a**) the pyramid case and its boundary condition; (**b**) MLS discretization with the red solid point representing the nodes.

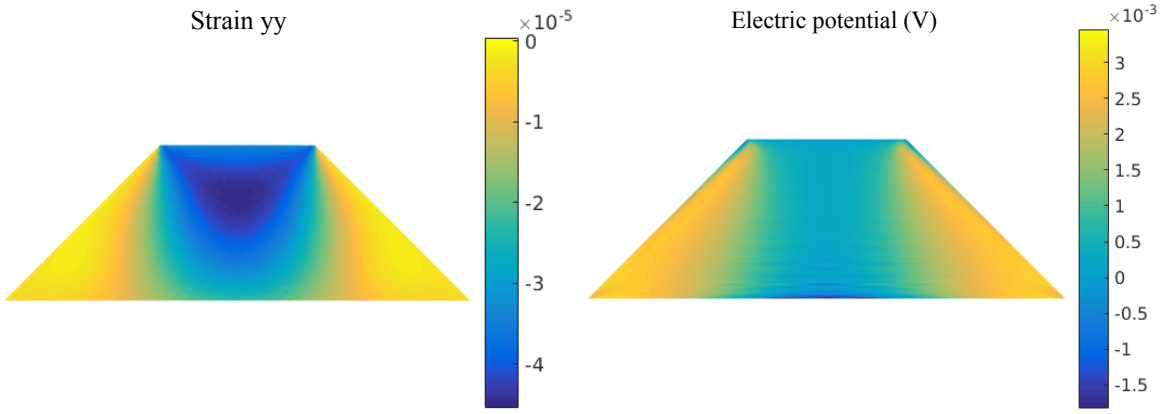


(**a**) Strain profile in the y direction (**b**) Electric potential (V)

**Figure 7.** Calculation result of the compressed truncated pyramid: (**a**) strain profile in the *y* direction; (**b**) electric field profile.

### *3.3. Flexoelectricity in Composite*

In this section, we demonstrate the possibility of inducing electric polarization in a composite system. The composite system is a combination of an embedding matrix in a square shape and a non-piezoelectric material (inclusion) in a circular shape, as shown in Figure 8. The composite under a

uniform mechanical loading induces electrical polarization due to the local strain gradients near the material discontinuity. The dielectric constant of the inclusion material is about 10% of the embedding matrix. It is assumed that the Young's modulus of the matrix material ($E_{mat}$) is lower than the Young's modulus of the inclusion material ($E_{inc}$). Three different Young's modulus ratios ($\frac{E_{inc}}{E_{mat}} = 10, 100, 1000$) are used to understand its influence on the energy transfer ratio between mechanical energy and electrical energy. The edge length of the square domain is $L$ = 10 µm with center inclusion radius $r_1$ = 1.5 µm. The remaining parameters (Table 1) for both materials are similar.

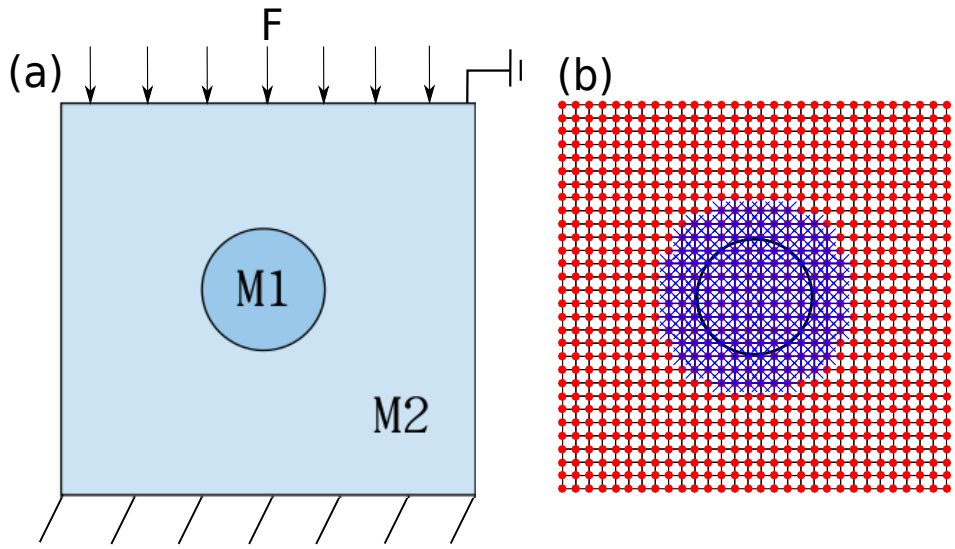


**Figure 8.** Schematic illustration of: (**a**) the square domain with center inclusion and its boundary condition; (**b**) MLS discretization with the red solid point representing the nodes and the blue asterisk representing the enriched nodes.

Figure 9 presents the strain and electric potential profile for the domain with a center inclusion. The non-uniform strain field near the inclusion boundary generates the polarization gradient and electric potential. Figure 10 plots the strain gradient profile: $\epsilon_{yy,y}$ and $\epsilon_{xx,x}$ along the horizontal and vertical center line of the square domain, respectively. In both directions, a high strain gradient is seen near the boundary of the inclusion, which is due to the different material toughness of the matrix and the inclusion. Since the inclusion material is a non-piezoelectric material, the induced electrical potential is a consequence of flexoelectricity. Therefore, the linear relationship between electrical potential and strain gradient generates the strong potential near the inclusion, as seen from Figure 9b.

In general, the volume percentage of the inclusions has a vast impact on the overall composite properties [56]. In order to investigate the volume percentage effect on the electromechanical coupling, we have repeated the simulations with many inclusions under the same loading condition. The number of inclusions is varied according to the area ratio from 0.5–2.5%. The area ratio is defined as the total area of inclusions divided by the area of a square domain. For each area ratio, several inclusion configurations (center location for inclusions) are examined, and later, the results are averaged. Note that, for inserting many inclusions, the radius is decreased to 0.4 µm. Figure 11a shows the strong electric potential near the inclusion boundary for a domain with 10 randomly-distributed inclusions. This is due to the non-uniform strain distributions near the inclusion boundary. A strong electric potential is noted in the region between the nearby inclusions. This corresponds to the interaction of the non-uniform strain fields around the neighboring inclusions. Figure 11b shows the mesh configuration. Figure 12 plots the variation of the total electrical energy transfer rate with the area ratio. The energy transfer increases with the increase of the inclusion area ratio. This behavior is expected since higher irregularities of strain are induced when many inclusions are present. Figure 12 also indicates that domains with an identical inclusion area ratio with higher $\frac{E_{inc}}{E_{mat}}$ induce higher energy

conversion from mechanical to electrical energy. This suggests that softer matrix materials enhance the electromechanical coupling characteristics.

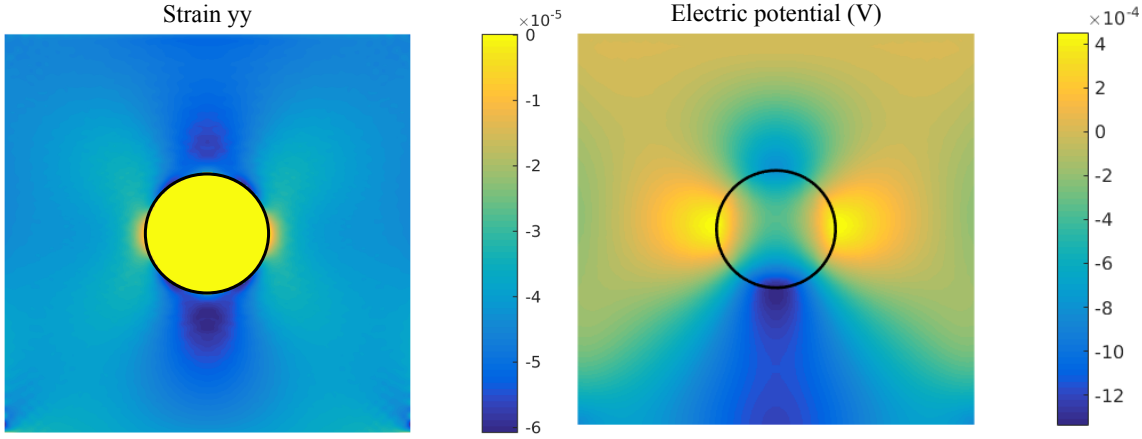


(**a**) Strain profile in the y direction (**b**) Induced electric potential (V)

**Figure 9.** Calculation results of a square composition under compression: (**a**) strain profile in the $y$ direction; (**b**) induced electric potential.

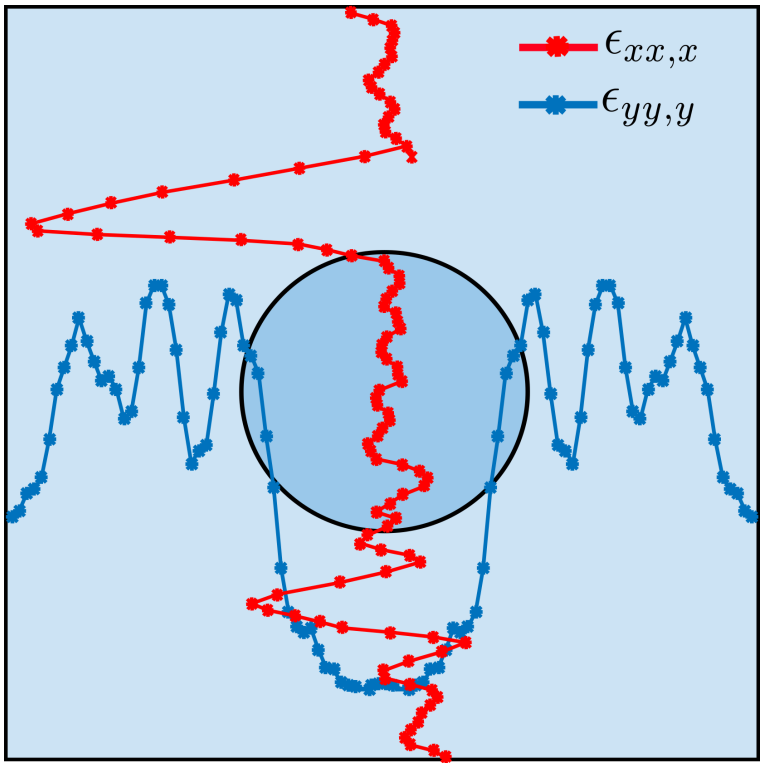


**Figure 10.** Strain gradient profile at the horizontal center line ($\epsilon_{yy,y}$) and the vertical center line ($\epsilon_{xx,x}$).

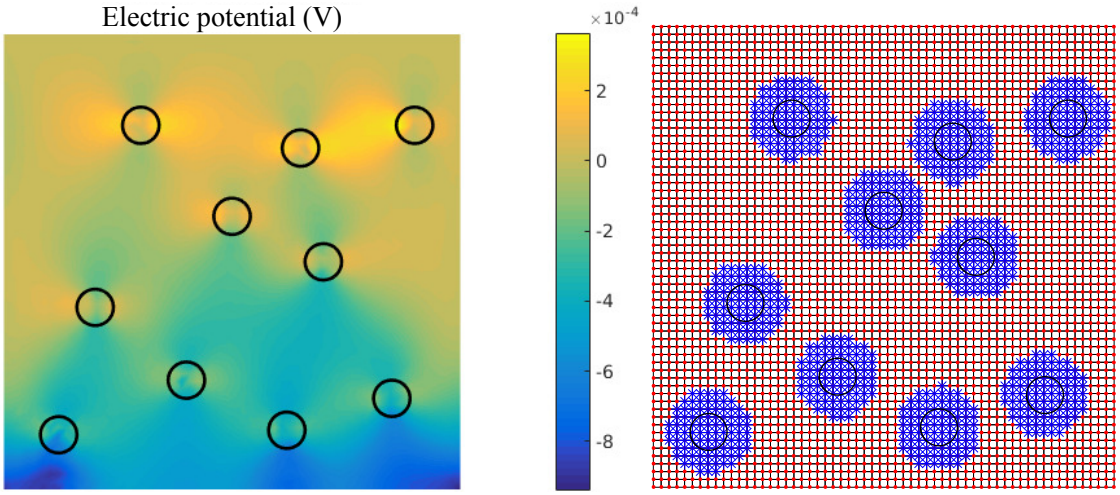


(**a**) Electric potential profile with ten inclusions (area ratio = 5.0%) (**b**) Mesh configuration

**Figure 11.** Calculation results of the square domain with randomly-distributed inclusions under compression: (**a**) electric potential profile for the domain with ten inclusions; (**b**) MLS discretization with the red solid point representing the nodes and the blue asterisk representing the enriched nodes.

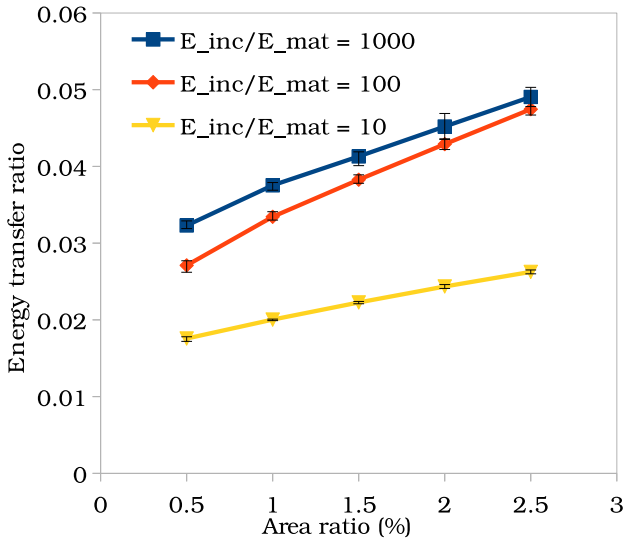


**Figure 12.** The energy conversion rate calculated by (Equation (14)) vs. the inclusion area ratio. Several setups are created for each configuration; hereafter, the averaged results are plotted. The error bar represents the upper and lower boundary of the calculation results.

## 4. Conclusions

In this study, the proposed model demonstrates the possibilities of inducing electromechanical coupling in a nano-composite material without the presence of the piezoelectric effect. The electromechanical coupling is modeled using the EFG method. Strain gradient involving partial differential equations is numerically solved using the MLS approximation. The $C^1$ continuity due to the strain gradient term is fulfilled by choosing the special weight function in the EFG. The level set techniques are employed to handle the weak discontinuity between the inclusion and matrix. The present numerical model captures the finite size flexoelectric effect for a mechanically-loaded cantilever beam. The converse flexoelectric effect-induced mechanical deformation of an electrically loaded cantilever beam is in good agreement with earlier reports. The results of the truncated pyramid

further validate the current model. The non-uniform strain fields near the inclusion boundary induce the electrical polarization and thus electric potential due to flexoelectricity. We also found that the magnitude of the electromechanical coupling is largely dependent on the area ratio between the inclusion and the matrix. The higher the inclusion area ratio, the stronger the electromechanical coupling. Furthermore, a softer matrix material can also enhance the electromechanical coupling when compared to a stiff material. These findings help in designing a nano-composite utilizing the flexoelectric effect.

**Author Contributions:** Conceptualization, B.H.; Methodology, B.H.; Software, B.H.; Validation, B.H.; Formal Analysis, B.H. and B.J.; Investigation, B.H. and B.J.; Resources, B.H. and B.J.; Data Curation, B.H. and B.J.; Writing-Original Draft Preparation, B.H. and B.J.; Writing-Review and Editing, B.H. and B.J.; Visualization, B.H. and B.J.; Supervision, X.Z.; Project Administration, X.Z.; Funding Acquisition, X.Z.

**Funding:** This research is funded by the National Science Foundation of China (11772234) and ERC Starting Grant 802205.

**Conflicts of Interest:** Authors declare no conflict of interest.

## Appendix A. Theory of Flexoelectricity

The enthalpy density $\mathcal{H}$ for a dielectric solid with piezoelectric and flexoelectric effects is [50,51]:

$$\mathcal{H}(\epsilon_{ij}, E_i, \epsilon_{jk,l}, E_{i,j}) = \frac{1}{2}\mathbb{C}_{ijkl}\epsilon_{ij}\epsilon_{kl} - e_{ikl}E_i\epsilon_{kl} + (d_{ijkl}E_{i,j}\epsilon_{kl} + f_{ijkl}E_i\epsilon_{jk,l}) - \frac{1}{2}\kappa_{ij}E_iE_j, \tag{A1}$$

where $E_i = -\phi_{,i}$ is the electric field; $\phi_i$ is the electric potential; $\epsilon_{ij}$ is the mechanical strain; $\mathbb{C}_{ijkl}$ is the fourth-order elastic moduli tensor; $e_{ikl}$ is the third-order tensor of piezoelectricity; $f_{iljk}$ and $d_{ijkl}$ are the fourth-order direct and converse flexoelectric tensors; and $\boldsymbol{\kappa}$ is the second-order dielectric tensor. Sharma et al. [52] defined the flexoelectric tensor $\mu_{ijkl}$ as the difference between $d_{iljk}$ and $f_{ijkl}$ by the application of integration by parts and Gauss divergence theorem to Equation (A1), which is:

$$\begin{aligned}
\int_\Omega \left(d_{ijkl}E_{i,j}\epsilon_{kl} + f_{ijkl}E_i\epsilon_{jk,l}\right) d\Omega &= \int_\Omega d_{ijkl}E_{i,j}\epsilon_{kl}d\Omega + \int_\Omega f_{ijkl}E_i\epsilon_{jk,l}d\Omega \\
&= \int_{\partial\Omega} d_{ijkl}E_i\epsilon_{kl}dS - \int_\Omega d_{ijkl}E_i\epsilon_{kl,j}d\Omega + \int_\Omega f_{ijkl}E_i\epsilon_{jk,l}d\Omega \\
&= -\int_\Omega \left(d_{ijkl}E_i\epsilon_{kl,j} - f_{ijkl}E_i\epsilon_{jk,l}\right) d\Omega + \int_{\partial\Omega} d_{ijkl}E_i\epsilon_{kl}dS \\
&= -\int_\Omega \left(d_{iljk} - f_{ijkl}\right) E_i\epsilon_{jk,l}d\Omega + \int_{\partial\Omega} d_{ijkl}E_i\epsilon_{kl}dS \\
&= -\int_\Omega \mu_{ijkl}E_i\epsilon_{jk,l}d\Omega + \int_{\partial\Omega} d_{ijkl}E_i\epsilon_{kl}dS.
\end{aligned} \tag{A2}$$

Rewriting Equation (A1) leads to Equation (1).

The stress $(\hat{\sigma}_{ij})$ and electric displacement $(\hat{D}_i)$ from Equation (1) when considering the piezoelectricity effect is given as:

$$\hat{\sigma}_{ij} = \frac{\partial\mathcal{H}}{\partial\epsilon_{ij}}; \qquad \hat{D}_i = -\frac{\partial\mathcal{H}}{\partial E_i}. \tag{A3}$$

Due to the presence of flexoelectricity, the higher-order stress $(\bar{\sigma}_{ijk})$ and electric displacement $(\bar{D}_{ij})$ read:

$$\bar{\sigma}_{ijk} = \frac{\partial\mathcal{H}}{\partial\epsilon_{ij,k}}; \qquad \bar{D}_{ij} = -\frac{\partial\mathcal{H}}{\partial E_{i,j}}. \tag{A4}$$

The total stress and electric displacement from piezoelectric and flexoelectric effects are summarized as:

$$\begin{aligned}
\sigma_{ij} &= \hat{\sigma}_{ij} - \bar{\sigma}_{ijk,k} = \mathbb{C}_{ijkl}\epsilon_{kl} - e_{kij}E_k + \mu_{lijk}E_{l,k}; \\
D_i &= \hat{D}_i - \bar{D}_{ij,j} = e_{ikl}\epsilon_{kl} + \kappa_{ij}E_j + \mu_{ijkl}\epsilon_{jk,l}.
\end{aligned} \tag{A5}$$

The essential and natural electric boundary condition are:

$$\begin{aligned} &\phi = \bar{\phi} \qquad \text{on} \quad \Gamma_\phi; \\ &D_i n_i = -w \qquad \text{on} \quad \Gamma_D; \\ &\Gamma_\phi \cup \Gamma_D = \partial\Omega \quad \text{and} \quad \Gamma_\phi \cap \Gamma_D = \emptyset, \end{aligned} \tag{A6}$$

where $\bar{\phi}$ and $w$ are the applied electric potential and surface charge density, $\partial\Omega$ represents the boundary of the domain, and $n_i$ is the unit normal to the boundary $\partial\Omega$. The mechanical boundary conditions are given as:

$$\begin{aligned} &u = \bar{u} \qquad \text{on} \quad \Gamma_u; \\ &t_k = \bar{t}_k \qquad \text{on} \quad \Gamma_t; \\ &\Gamma_u \cup \Gamma_t = \partial\Omega \quad \text{and} \quad \Gamma_u \cap \Gamma_t = \emptyset, \end{aligned} \tag{A7}$$

where $\bar{u}$ and $\bar{t}_k$ are prescribed mechanical displacement and traction. The remaining boundary conditions (normal derivation of displacement and higher-order tractions) resulting from the strain gradient have been set to zero under the assumption of a homogeneous condition.

Rewrite Equations (A3) and (A4) as:

$$\begin{aligned} \partial\mathcal{H} &= \hat{\sigma}_{ij}\partial\epsilon_{ij} \\ \partial\mathcal{H} &= \bar{\sigma}_{ijk}\partial\epsilon_{ij,k}, \\ \partial\mathcal{H} &= -\hat{D}_i\partial E_i \end{aligned} \tag{A8}$$

and integration over the domain $\Omega$ gives:

$$\boldsymbol{H} = \frac{1}{2}\int_\Omega \left(\hat{\sigma}_{ij}\epsilon_{ij} + \bar{\sigma}_{ijk}\epsilon_{ij,k} - \hat{D}_i E_i\right) d\Omega, \tag{A9}$$

where $\boldsymbol{H}$ is the total electrical enthalpy. The external work by surface mechanical and electrical forces is given by:

$$\boldsymbol{W}_{ext} = \int_{\Gamma_t} \bar{t}_i u_i dS - \int_{\Gamma_D} w\phi dS. \tag{A10}$$

Finally, the weak form of the mechanical and electrical equilibrium derived from the Hamilton principle for the static problem yields:

$$0 = \int_\Omega \left(\hat{\sigma}_{ij}\delta\epsilon_{ij} + \bar{\sigma}_{ijk}\delta\epsilon_{ij,k} - \hat{D}_i\delta E_i\right) d\Omega - \int_{\Gamma_t} \bar{t}_i\delta u_i dS - \int_{\Gamma_D} w\delta\phi dS. \tag{A11}$$

Substituting Equations (A3)–(A5) into Equation (A11) yields:

$$\begin{aligned} &\int_\Omega \left(\mathbb{C}_{ijkl}\delta\epsilon_{ij}\epsilon_{kl} - e_{kij}E_k\delta\epsilon_{ij} - \mu_{lijk}E_l\delta\epsilon_{ij,k} - \kappa_{ij}\delta E_i E_j - e_{ikl}\delta E_i\epsilon_{kl} - \mu_{ijkl}\delta E_i\epsilon_{jk,l}\right) d\Omega \\ &- \int_{\Gamma_t} \bar{t}_i\delta u_i dS - \int_{\Gamma_D} w\delta\phi dS = 0\,. \end{aligned} \tag{A12}$$

The unknowns (displacement and electric potential) in Equation (A12) are approximated using MLS.

## Appendix B. Details of the Shape Function

The shape function $\Phi_I(x)$ associates with Node I and a point $x$ under MLS is:

$$\Phi_I(x) = \boldsymbol{p}^T(x)\,[\boldsymbol{A}(x)]^{-1}\,w\,(x - x_I)\,\boldsymbol{p}(x_I), \tag{A13}$$

where $\boldsymbol{p}(x)$ is the second-order polynomial, which is:

$$\boldsymbol{p}^T(x) = \left[1\ x\ y\ x^2\ xy\ y^2\right]. \tag{A14}$$

The quadratic spline weight function $w$ ensures $C^3$ continuity inside an element and $C^2$ continuity between elements [40]. The mathematical expression for $w$ is:

$$w(r) = \begin{cases} 1 - 6r^2 + 8r^3 - 3r^4 & \text{if } r \le 1 \\ 0 & \text{if } r > 1 \end{cases} \tag{A15}$$

where:

$$r = \frac{\parallel x_I - x \parallel}{d}\ , \tag{A16}$$

$d$ is the predefined search radius of the support domain and $d$ equals three-times the nodal spacing. The moment matrix $\boldsymbol{A}(x)$ has the form:

$$\boldsymbol{A}(\boldsymbol{x}) = \sum_{I=1}^{N} w(x - x_I)\boldsymbol{p}(x_I)\boldsymbol{p}^T(x_I)\ . \tag{A17}$$

A sufficient number of support nodes ensures the non-singularity of matrix $\boldsymbol{A}(x)$. The enrichment function $\Psi(x)$ has the form [42]:

$$\Psi(x) = \text{abs}(\psi(x)); \qquad \text{where } \psi(x) = \min_{i=1,2,\ldots,n_c} \left\{ \parallel x - x_c^i \parallel - r_c^i \right\} \tag{A18}$$

where $n_c$ is the total number of inclusions inside the domain, $x_c^i$ is the center coordinate of the $i^{\text{th}}$ circular inclusion, and $r_c^i$ is the radius of the $i^{\text{th}}$ circular inclusion.

## Appendix C. Mathematical Expression for the Elements in Equation (4)

$$\boldsymbol{B}_u = \partial\boldsymbol{\Phi}_u = \begin{bmatrix} \frac{\partial}{\partial x} & 0 & \frac{\partial}{\partial y} \\ 0 & \frac{\partial}{\partial y} & \frac{\partial}{\partial x} \end{bmatrix}\ ; \tag{A19}$$

$$\boldsymbol{B}_\phi = \partial\boldsymbol{\Phi}_\phi = \begin{bmatrix} \frac{\partial}{\partial x} & \frac{\partial}{\partial y} \end{bmatrix}\ ; \tag{A20}$$

$$\boldsymbol{H}_u = \partial\partial\boldsymbol{\Phi}_u = \begin{bmatrix} \frac{\partial^2}{\partial x^2} & 0 & \frac{\partial^2}{\partial x \partial y} & \frac{\partial^2}{\partial x \partial y} & 0 & \frac{\partial^2}{\partial y^2} \\ 0 & \frac{\partial^2}{\partial x \partial y} & \frac{\partial^2}{\partial x^2} & 0 & \frac{\partial^2}{\partial y^2} & \frac{\partial^2}{\partial x \partial y} \end{bmatrix}\ ; \tag{A21}$$

$$\boldsymbol{B}_u^{enr} = \partial\boldsymbol{\Phi}_u\boldsymbol{\Psi} + \boldsymbol{\Phi}_u\partial\boldsymbol{\Psi}\ ; \tag{A22}$$

$$\boldsymbol{B}_\phi^{enr} = \partial\boldsymbol{\Phi}_\phi\boldsymbol{\Psi} + \boldsymbol{\Phi}_\phi\partial\boldsymbol{\Psi}\ ; \tag{A23}$$

$$\boldsymbol{H}_u^{enr} = \partial\partial\boldsymbol{\Phi}_u\boldsymbol{\Psi} + \boldsymbol{\Phi}_u\partial\partial\boldsymbol{\Psi} + 2\partial\boldsymbol{\Phi}_u\partial\boldsymbol{\Psi}\ ; \tag{A24}$$

$$\boldsymbol{B}_u^{enr} = \begin{bmatrix} \frac{\partial}{\partial x}\psi(x) + \text{sign}(\psi(x))\frac{(x-x_c)}{d} & 0 \\ 0 & \frac{\partial}{\partial x}\psi(x) + \text{sign}(\psi(x))\frac{(y-y_c)}{d} \\ \frac{\partial}{\partial x}\psi(x) + \text{sign}(\psi(x))\frac{(y-y_c)}{d} & \frac{\partial}{\partial x}\psi(x) + \text{sign}(\psi(x))\frac{(x-x_c)}{d} \end{bmatrix}^T ; \tag{A25}$$

$$\boldsymbol{B}_\phi^{enr} = \begin{bmatrix} \frac{\partial}{\partial x}\psi(x) + \text{sign}(\psi(x))\frac{(x-x_c)}{d} \\ \frac{\partial}{\partial x}\psi(x) + \text{sign}(\psi(x))\frac{(y-y_c)}{d} \end{bmatrix}^T ; \tag{A26}$$

$$\boldsymbol{H}_u^{enr} = \begin{bmatrix} \frac{\partial^2}{\partial x^2}\psi(x) + 2\frac{\partial}{\partial x}\text{sign}(\psi(x))\frac{(x-x_c)}{d} + \text{sign}(\psi(x))\frac{(y-y_c)^2}{d^{(\frac{3}{2})}} & 0 \\ 0 & \frac{\partial^2}{\partial y \partial x}\psi(x) + \frac{\partial}{\partial y}\text{sign}(\psi(x))\frac{(x-x_c)}{d} + \frac{\partial}{\partial x}\text{sign}(\psi(x))\frac{(y-y_c)}{d} + \text{sign}(\psi(x))\frac{-(x-x_c)*(y-y_c)}{d^{(\frac{3}{2})}} \\ \frac{\partial^2}{\partial y \partial x}\psi(x) + \frac{\partial}{\partial y}\text{sign}(\psi(x))\frac{(x-x_c)}{d} + \frac{\partial}{\partial x}\text{sign}(\psi(x))\frac{(y-y_c)}{d} + \text{sign}(\psi(x))\frac{-(x-x_c)*(y-y_c)}{d^{(\frac{3}{2})}} & \frac{\partial^2}{\partial x^2}\psi(x) + 2\frac{\partial}{\partial x}\text{sign}(\psi(x))\frac{(x-x_c)}{d} + \text{sign}(\psi(x))\frac{(y-y_c)^2}{d^{(\frac{3}{2})}} \\ 0 & \frac{\partial^2}{\partial y^2}\psi(x) + 2\frac{\partial}{\partial y}\text{sign}(\psi(x))\frac{(y-y_c)}{d} + \text{sign}(\psi(x))\frac{(x-x_c)^2}{d^{(\frac{3}{2})}} \\ \frac{\partial^2}{\partial y^2}\psi(x) + 2\frac{\partial}{\partial y}\text{sign}(\psi(x))\frac{(y-y_c)}{d} + \text{sign}(\psi(x))\frac{(x-x_c)^2}{d^{(\frac{3}{2})}} & \frac{\partial^2}{\partial y \partial x}\psi(x) + \frac{\partial}{\partial y}\text{sign}(\psi(x))\frac{(x-x_c)}{d} + \frac{\partial}{\partial x}\text{sign}(\psi(x))\frac{(y-y_c)}{d} + \text{sign}(\psi(x))\frac{-(x-x_c)*(y-y_c)}{d^{(\frac{3}{2})}} \end{bmatrix}^T . \tag{A27}$$

## References


1. Chen, J.; Qiu, Q.; Han, Y.; Lau, D. Piezoelectric materials for sustainable building structures: Fundamentals and applications. *Renew. Sustain. Energy Rev.* **2019**, *101*, 14–25. [CrossRef]
2. Cabeza, L.F.; Barreneche, C.; Miró, L.; Morera, J.M.; Bartolí, E.; Fernández, A.I. Low carbon and low embodied energy materials in buildings: A review. *Renew. Sustain. Energy Rev.* **2013**, *23*, 536–542. [CrossRef]
3. Ramesh, T.; Prakash, R.; Shukla, K. Life cycle energy analysis of buildings: An overview. *Energy Build.* **2010**, *42*, 1592–1600. [CrossRef]
4. Scopelianos, A.G. Piezoelectric Biomedical Device. US Patent 5,522,879, 4 June 1996.
5. Zhou, Q.; Lau, S.; Wu, D.; Shung, K.K. Piezoelectric films for high frequency ultrasonic transducers in biomedical applications. *Prog. Mater. Sci.* **2011**, *56*, 139–174. [CrossRef] [PubMed]
6. Jiang, X.; Huang, W.; Zhang, S. Flexoelectric nano-generator: Materials, structures and devices. *Nano Energy* **2013**, *2*, 1079–1092. [CrossRef]
7. Zhuang, X.Y.; Huang, R.Q.; Liang, C.; Rabczuk, T. A coupled thermo-hydro-mechanical model of jointed hard rock for compressed air energy storage. *Math. Probl. Eng.* **2014**, *2014*, 179169. [CrossRef]
8. Ahmadpoor, F.; Sharma, P. Flexoelectricity in two-dimensional crystalline and biological membranes. *Nanoscale* **2015**, *7*, 16555–16570. [CrossRef]
9. Ma, W.; Cross, L.E. Observation of the flexoelectric effect in relaxor Pb (Mg 1/3 Nb 2/3) O 3 ceramics. *Appl. Phys. Lett.* **2001**, *78*, 2920–2921. [CrossRef]
10. Ma, W.; Cross, L.E. Flexoelectricity of barium titanate. *Appl. Phys. Lett.* **2006**, *88*, 232902. [CrossRef]
11. Hong, J.; Catalan, G.; Scott, J.; Artacho, E. The flexoelectricity of barium and strontium titanates from first principles. *J. Phys. Condens. Matter* **2010**, *22*, 112201. [CrossRef]
12. Xu, T.; Wang, J.; Shimada, T.; Kitamura, T. Direct approach for flexoelectricity from first-principles calculations: Cases for SrTiO3 and BaTiO3. *J. Phys. Condens. Matter* **2013**, *25*, 415901. [CrossRef] [PubMed]
13. Kundalwal, S.; Meguid, S.; Weng, G. Strain gradient polarization in graphene. *Carbon* **2017**, *117*, 462–472. [CrossRef]
14. Javvaji, B.; He, B.; Zhuang, X. The generation of piezoelectricity and flexoelectricity in graphene by breaking the materials symmetries. *Nanotechnology* **2018**, *29*, 225702. [CrossRef] [PubMed]
15. He, B.; Javvaji, B.; Zhuang, X. Size dependent flexoelectric and mechanical properties of barium titanate nanobelt: A molecular dynamics study. *Phys. B Condens. Matter* **2018**, *545*, 527–535. [CrossRef]
16. Zhang, Z.; Geng, D.; Wang, X. Calculation of the piezoelectric and flexoelectric effects in nanowires using a decoupled finite element analysis method. *J. Appl. Phys.* **2016**, *119*, 154104. [CrossRef]
17. Nanthakumar, S.; Zhuang, X.; Park, H.S.; Rabczuk, T. Topology optimization of flexoelectric structures. *J. Mech. Phys. Solids* **2017**, *105*, 217–234. [CrossRef]
18. Nanthakumar, S.S.; Lahmer, T.; Zhuang, X.Y.; Zi, G.; Rabczuk, T. Detection of material interfaces using a regularized level set method in piezoelectric structures. *Inverse Probl. Sci. Eng.* **2016**, *24*, 153–176. [CrossRef]
19. Deng, F.; Deng, Q.; Yu, W.; Shen, S. Mixed Finite Elements for Flexoelectric Solids. *J. Appl. Mech.* **2017**, *84*, 081004. [CrossRef]
20. Mao, S.; Purohit, P.K.; Aravas, N. Mixed finite-element formulations in piezoelectricity and flexoelectricity. *Proc. R. Soc. A* **2016**, *472*, 20150879. [CrossRef]
21. Ghasemi, H.; Park, H.S.; Rabczuk, T. A level-set based IGA formulation for topology optimization of flexoelectric materials. *Comput. Methods Appl. Mech. Eng.* **2017**, *313*, 239–258. [CrossRef]
22. Hamdia, K.M.; Ghasemi, H.; Zhuang, X.Y.; Alajlan, N.; Rabczuk, T. Sensitivity and uncertainty analysis for flexoelectric nanostructures. *Comput. Methods Appl. Mech. Eng.* **2018**, *337*, 95–109. [CrossRef]
23. Nguyen-Thanh, N.; Valizadeh, N.; Nguyen, M.N.; Nguyen-Xuan, H.; Zhuang, X.Y.; Areias, P.; Zi, G.; Bazilevs, Y.; De Lorenzis, L.; Rabczuk, T. An extended isogeometric thin shell analysis based on Kirchhoff–Love theory. *Comput. Methods Appl. Mech. Eng.* **2015**, *284*, 265–291. [CrossRef]
24. Nguyen, V.P.; Anitescu, C.; Bordas, S.P.; Rabczuk, T. Isogeometric analysis: An overview and computer implementation aspects. *Math. Comput. Simul.* **2015**, *117*, 89–116. [CrossRef]
25. Hughes, T.J.; Cottrell, J.A.; Bazilevs, Y. Isogeometric analysis: CAD, finite elements, NURBS, exact geometry and mesh refinement. *Comput. Methods Appl. Mech. Eng.* **2005**, *194*, 4135–4195. [CrossRef]
26. Abdollahi, A.; Peco, C.; Millán, D.; Arroyo, M.; Arias, I. Computational evaluation of the flexoelectric effect in dielectric solids. *J. Appl. Phys.* **2014**, *116*, 093502. [CrossRef]

27. Abdollahi, A.; Millán, D.; Peco, C.; Arroyo, M.; Arias, I. Revisiting pyramid compression to quantify flexoelectricity: A three-dimensional simulation study. *Phys. Rev. B* **2015**, *91*, 104103. [CrossRef]
28. Bernholc, J.; Nakhmanson, S.M.; Nardelli, M.B.; Meunier, V. Understanding and enhancing polarization in complex materials. *Comput. Sci. Eng.* **2004**, *6*, 12–21. [CrossRef]
29. Ghidelli, M.; Sebastiani, M.; Collet, C.; Guillemet, R. Determination of the elastic moduli and residual stresses of freestanding Au-TiW bilayer thin films by nanoindentation. *Mater. Des.* **2016**, *106*, 436–445. [CrossRef]
30. Msekh, M.A.; Cuong, N.H.; Zi, G.; Areias, P.; Zhuang, X.Y.; Rabczuk, T. Fracture properties prediction of clay/epoxy nanocomposites with interphase zones using a phase field model. *Eng. Fract. Mech.* **2018**, *188*, 287–299. [CrossRef]
31. Bhavanasi, V.; Kumar, V.; Parida, K.; Wang, J.; Lee, P.S. Enhanced Piezoelectric Energy Harvesting Performance of Flexible PVDF-TrFE Bilayer Films with Graphene Oxide. *ACS Appl. Mater. Interfaces* **2016**, *8*, 521–529. [CrossRef]
32. Biswal, A.K.; Das, S.; Roy, A. Designing and synthesis of a polymer matrix piezoelectric composite for energy harvesting. *IOP Conf. Ser. Mater. Sci. Eng.* **2017**, *178*, 012002, doi:10.1088/1742-6596/755/1/011001. [CrossRef]
33. Sidhardh, S.; Ray, M.C. Effective properties of flexoelectric fiber-reinforced nanocomposite. *Mater. Today Commun.* **2018**, *17*, 114–123. [CrossRef]
34. Hamdia, K.M.; Silani, M.; Zhuang, X.Y.; He, P.F.; Rabczuk, T. Stochastic analysis of the fracture toughness of polymeric nanoparticle composites using polynomial chaos expansions. *Int. J. Fract.* **2017**, *206*, 215–227. [CrossRef]
35. Ghasemi, H.; Park, H.S.; Rabczuk, T. A multi-material level set-based topology optimization of flexoelectric composites. *Comput. Methods Appl. Mech. Eng.* **2018**, *332*, 47–62. [CrossRef]
36. Cordes, L.; Moran, B. Treatment of material discontinuity in the element-free Galerkin method. *Comput. Methods Appl. Mech. Eng.* **1996**, *139*, 75–89. [CrossRef]
37. Rabczuk, T.; Belytschko, T.; Xiao, S.P. Stable particle methods based on Lagrangian kernels. *Comput. Methods Appl. Mech. Eng.* **2004**, *193*, 1035–1063. [CrossRef]
38. Krongauz, Y.; Belytschko, T. EFG approximation with discontinuous derivatives. *Int. J. Numer. Methods Eng.* **1998**, *41*, 1215–1233. [CrossRef]
39. Rabczuk, T.; Zi, G.; Bordas, S.; Nguyen-Xuan, H. A geometrically non-linear three-dimensional cohesive crack method for reinforced concrete structures. *Eng. Fract. Mech.* **2008**, *75*, 4740–4758. [CrossRef]
40. Nguyen, V.P.; Rabczuk, T.; Bordas, S.; Duflot, M. Meshless methods: A review and computer implementation aspects. *Math. Comput. Simul.* **2008**, *79*, 763–813. [CrossRef]
41. Budarapu, P.R.; Gracie, R.; Yang, S.W.; Zhuang, X.Y.; Rabczuk, T. Efficient coarse graining in multiscale modeling of fracture. *Theor. Appl. Fract. Mech.* **2014**, *69*, 126–143. [CrossRef]
42. Sukumar, N.; Chopp, D.L.; Moës, N.; Belytschko, T. Modeling holes and inclusions by level sets in the extended finite-element method. *Comput. Methods Appl. Mech. Eng.* **2001**, *190*, 6183–6200. [CrossRef]
43. Ren, H.L.; Zhuang, X.Y.; Rabczuk, T. Dual-horizon peridynamics: A stable solution to varying horizons. *Comput. Methods Appl. Mech. Eng.* **2017**, *318*, 762–782. [CrossRef]
44. Ren, H.L.; Zhuang, X.Y.; Cai, Y.C.; Rabczuk, T. Dual-horizon peridynamics. *Int. J. Numer. Methods Eng.* **2016**, *108*, 1451–1476. [CrossRef]
45. Rabczuk, T.; Bordas, S.; Zi, G. On three-dimensional modelling of crack growth using partition of unity methods. *Comput. Struct.* **2010**, *88*, 1391–1411. [CrossRef]
46. Rabczuk, T.; Areias, P.M.A.; Belytschko, T. A meshfree thin shell method for non-linear dynamic fracture. *Int. J. Numer. Methods Eng.* **2007**, *72*, 524–548. [CrossRef]
47. Rabczuk, T.; Belytschko, T. A three-dimensional large deformation meshfree method for arbitrary evolving cracks. *Comput. Methods Appl. Mech. Eng.* **2007**, *196*, 2777–2799. [CrossRef]
48. Rabczuk, T.; Belytschko, T. Cracking particles: A simplified meshfree method for arbitrary evolving cracks. *Int. J. Numer. Methods Eng.* **2004**, *61*, 2316–2343. [CrossRef]
49. Rabczuk, T.; Bordas, S.; Zi, G. A three-dimensional meshfree method for continuous multiple-crack initiation, propagation and junction in statics and dynamics. *Comput. Mech.* **2007**, *40*, 473–495. [CrossRef]
50. Majdoub, M.; Sharma, P.; Cagin, T. Enhanced size-dependent piezoelectricity and elasticity in nanostructures due to the flexoelectric effect. *Phys. Rev. B* **2008**, *77*, 125424. [CrossRef]

51. Majdoub, M.S.; Sharma, P.; Çağin, T. Erratum: Enhanced size-dependent piezoelectricity and elasticity in nanostructures due to the flexoelectric effect [Phys. Rev. B 77, 125424 (2008)]. *Phys. Rev. B* **2009**, *79*, 119904, doi:10.1103/PhysRevB.79.119904. [CrossRef]
52. Sharma, N.; Landis, C.; Sharma, P. Piezoelectric thin-film superlattices without using piezoelectric materials. *J. Appl. Phys.* **2010**, *108*, 024304. [CrossRef]
53. Belytschko, T.; Lu, Y.Y.; Gu, L. Element-free Galerkin methods. *Int. J. Numer. Methods Eng.* **1994**, *37*, 229–256. [CrossRef]
54. Belytschko, T.; Lu, Y.; Gu, L.; Tabbara, M. Element-free Galerkin methods for static and dynamic fracture. *Int. J. Solids Struct.* **1995**, *32*, 2547–2570. [CrossRef]
55. Belytschko, T.; Black, T. Elastic crack growth in finite elements with minimal remeshing. *Int. J. Numer. Methods Eng.* **1999**, *45*, 601–620. [CrossRef]
56. He, B.; Mortazavi, B.; Zhuang, X.; Rabczuk, T. Modeling Kapitza resistance of two-phase composite material. *Compos. Struct.* **2016**, *152*, 939–946. [CrossRef]